

Nonlinear reflection process of linearly polarized, broadband Alfvén waves in the fast solar wind

M. Shoda and T. Yokoyama

Department of Earth and Planetary Science, The University of Tokyo, Bunkyo-ku, Tokyo
113-0033, Japan

shoda@eps.s.u-tokyo.ac.jp

Received _____; accepted _____

ABSTRACT

Using one-dimensional numerical simulations, we study the elementary process of Alfvén wave reflection in a uniform medium, including nonlinear effects. In the linear regime, Alfvén wave reflection is triggered only by the inhomogeneity of the medium, whereas in the nonlinear regime, it can occur via nonlinear wave-wave interactions. Such nonlinear reflection (backscattering) is typified by decay instability. In most studies of decay instabilities, the initial condition has been a circularly polarized Alfvén wave. In this study we consider a linearly polarized Alfvén wave, which drives density fluctuations by its magnetic pressure force. For generality, we also assume a broadband wave with a red-noise spectrum. In the data analysis, we decompose the fluctuations into characteristic variables using local eigenvectors, thus revealing the behaviors of the individual modes. Different from circular-polarization case, we find that the wave steepening produces a new energy channel from the parent Alfvén wave to the backscattered one. Such nonlinear reflection explains the observed increasing energy ratio of the sunward to the anti-sunward Alfvénic fluctuations in the solar wind with distance against the dynamical alignment effect.

Subject headings: magnetohydrodynamics(MHD) — methods: numerical — Sun: corona — Sun: solar wind — Sun: Alfvén wave

1. Introduction

Alfvén waves are frequently observed in the solar atmosphere (De Pontieu et al. 2007; Okamoto et al. 2007). As Alfvén waves upwardly transport large amounts of photospheric kinetic energy (Fujimura & Tsuneta 2009), they are considered promising sources of coronal heating and acceleration of fast solar wind in coronal holes. In this framework, rapid dissipation of Alfvén waves should inject thermal energy into the corona and accelerate the solar wind via wave pressure (Dewar 1970; Belcher 1971; Hollweg 1973; Jacques 1977; Heinemann & Olbert 1980). As the magnetic flux tubes expand in the coronal hole region, the nonlinearity of the Alfvén waves become significantly large so that nonlinear interactions can initiate an energy cascade, playing a significant role in the dissipation process.

Nonlinear dissipation of Alfvén waves can occur by two main candidate mechanisms: compressible and incompressible processes. In the first mechanism, nonlinear coupling between Alfvén and compressible waves initiate an energy cascade by steepening. Unless they are monochromatic and circularly polarized, Alfvén waves can generate acoustic waves via their magnetic pressure forces (Hollweg 1971), which then steepen into shock waves. Alfvén waves can also directly steepen to form fast (switch-on) shocks or rotational discontinuities (Montgomery 1959; Cohen & Kulsrud 1974; Kennel et al. 1990). This steepening and mode conversion process are suggested to explain many solar phenomena such as spicule formation (Hollweg et al. 1982; Kudoh & Shibata 1999; Matsumoto & Shibata 2010), coronal heating (Moriyasu et al. 2004; Suzuki & Inutsuka 2005, 2006; Antolin et al. 2008; Matsumoto & Suzuki 2014), and solar wind acceleration (Suzuki & Inutsuka 2005, 2006; Matsumoto & Suzuki 2014).

The second mechanism is Alfvénic turbulence triggered by two bidirectional Alfvén waves (Iroshnikov 1964; Kraichnan 1965; Goldreich & Sridhar 1995). Due to nonuniform Alfvén speed in coronal holes, Alfvén waves generated by photospheric

motion are linearly reflected (Ferraro & Plumpton 1958; An et al. 1990; Velli 1993; Cranmer & van Ballegooijen 2005; Hollweg & Isenberg 2007). The resulting interaction between the original anti-sunward and reflected sunward waves triggers Alfvénic turbulence. This turbulence model is also suggested as a candidate for coronal heating and solar wind acceleration (Cranmer et al. 2007; Verdini et al. 2010) using a phenomenological turbulent dissipation mode (Hossain et al. 1995; Dmitruk et al. 2002; Chandran et al. 2009). As shown in recent three-dimensional direct numerical simulations using a reduced magnetohydrodynamics (MHD) approximation, Alfvénic turbulence can heat both closed coronal loops (van Ballegooijen et al. 2011) and open coronal holes (Woolsey & Cranmer 2015).

The amount of reflected wave energy flux is of critical importance in the Alfvénic turbulence models. Most studies on turbulence-driven coronal heating and solar wind acceleration have assumed locally incompressible (Zhou & Matthaeus 1990) or nearly incompressible (Zank & Matthaeus 1992) plasma. However, Alfvén waves can be reflected by nonlinear interactions with compressible waves. The best-known example of such nonlinear reflection is the decay instability (Sagdeev & Galeev 1969; Goldstein 1978; Hoshino & Goldstein 1989; Del Zanna et al. 2001). In addition, Suzuki & Inutsuka (2005) investigated a compressible heating/acceleration model and reported significant reflection of Alfvén waves. Therefore the role of compressibility in reflection triggering should not be discounted. To more realistically model the corona and solar wind, it is necessary to elucidate the elementary processes of Alfvén wave reflection caused by nonlinear interactions with compressible modes. This problem has motivated the study in this paper.

Belcher & Davis (1971) reported that solar wind fluctuations near Earth’s orbit are mainly composed of anti-sunward Alfvén waves. Later studies revealed that the ratio of sunward to anti-sunward Alfvén wave energies increases with distance (Bavassano et al.

2000). This fact is against the fundamental process of Alfvénic turbulence called dynamical alignment (Dobrowolny et al. 1980). To explain this trend, researchers have proposed theoretical models based on the compressible turbulence (Grappin et al. 1993), linear reflection (Verdini & Velli 2007) and decay instability (Del Zanna et al. 2001).

Herein, we propose a new reflection process that explains this observational fact. This process is a combination of the wave steepening and the decay instability, that is, linear polarization and resultant steepening forms a new energy channel which never appears in the circular-polarization case. We show that our result with a proper scaling well agree with the observation by Bavassano et al. (2000).

The remainder of this paper is organized as follows. In § 2 we describe the numerical setting and data analysis method. The results of the numerical calculation and data analysis are presented in § 3. In the last section, § 4, we propose an elementary reflection process that can explain our results and discuss on the comparison with the observation.

2. Method

2.1. Numerical setting

For simplicity, we assume a one-dimensional Cartesian coordinate system. Periodic boundary conditions are used. We denote by x the spatial coordinate, background magnetic field \mathbf{B}_0 parallel to the x axis. Because the sole transverse component is the y component, the Alfvén waves are linearly polarized. We also assume a static background with a uniform density ρ_0 and uniform magnetic field B_0 . The initial state can then expressed as

$$\rho = \rho_0, \quad v_x = 0, \quad v_y = 0, \quad B_x = B_0, \quad B_y = 0. \quad (1)$$

The dissipation mechanisms, such as viscosity and resistivity, are not explicitly stated. For brevity, we further assume an isothermal system with speed of sound C_s . The basic equations of the system are thus given by

$$\frac{\partial}{\partial t}\rho + \frac{\partial}{\partial x}(\rho v_x) = 0, \quad (2)$$

$$\frac{\partial}{\partial t}(\rho v_x) + \frac{\partial}{\partial x}\left(\rho v_x^2 + \rho C_s^2 + \frac{B_y^2}{8\pi}\right) = 0, \quad (3)$$

$$\frac{\partial}{\partial t}(\rho v_y) + \frac{\partial}{\partial x}\left(\rho v_x v_y - \frac{B_0 B_y}{4\pi}\right) = 0, \quad (4)$$

$$\frac{\partial}{\partial t}B_y + \frac{\partial}{\partial x}(B_y v_x - B_0 v_y) = 0. \quad (5)$$

The equations are numerically solved by using an upwind scheme with the linearized Riemann solver (Roe’s solver) developed for isothermal MHD systems by Nakajima & Hanawa (1996) and Fukuda & Hanawa (1999). The spatial and temporal accuracies in this scheme are set to be second-order, and unphysical numerical oscillations near the discontinuities are avoided by a minmod flux limiter.

2.2. Initial condition as the wave input

We input the waves by the initial condition. The fluctuations are denoted by Δ and initially exist as a purely rightward Elsässer state without fluctuations in ρ or v_x :

$$\Delta\rho = 0, \quad \Delta v_x = 0, \quad \Delta v_y = C_A f(x), \quad \Delta B_y = -B_0 f(x), \quad (6)$$

where $C_A = B_0/\sqrt{4\pi\rho_0}$ is the background Alfvén speed, and $f(x)$ represents the initial wave profile. Notice that if $f(x)$ is sufficiently small, the leftward Elsässer variable vanishes, and the initial condition becomes a purely rightward linear Alfvén wave.

The initial fluctuation is assumed to have a red-noise energy spectrum with random phase. Previous observations (Matsumoto & Shibata 2010) revealed that within a certain

band (typically with period between 1 min and 10 min), the energy spectrum of photospheric transverse motion approximates a red-noise spectrum. By setting the highest wavenumber of the initial fluctuation spectrum equal to one tenth of the Nyquist wavenumber, itself given as one-half of the spatial grid points N_x , $f(x)$ can be explicitly written as

$$f(x) = \sum_{n=1}^N A_n \sin \left[2\pi \left(\frac{nx}{L} \right) + \phi_n \right] \quad (7)$$

where $N = N_x/20$, $A_n = A_0 n^{-1}$ and L is the size of the simulation box. A_0 is the amplitude parameter, and ϕ_n is a random value ranging between 0 and 2π . We perform two kinds of simulations: short-term simulations up to $t = 20\tau_A$ with $N_x = 5000$ and long-term evolutions up to $t = 1000\tau_A$ with $N_x = 1000$ where $\tau_A = L/C_A$ is the Alfvén time of the simulation box. Our simulation is characterized by two free physical parameters: the plasma beta $\beta = (C_s/C_A)^2$ and the initial fluctuation energy E_{wave} , which is defined as follows:

$$\begin{aligned} E_{wave} &= \int_0^L dx \left[\frac{1}{2} \rho_0 \Delta v_y^2 + \frac{1}{8\pi} \Delta B_y^2 \right] \\ &= \frac{1}{2} \rho_0 (A_0 C_A)^2 L \sum_{n=1}^N n^{-2}. \end{aligned} \quad (8)$$

2.3. Decomposition of fluctuations into characteristic variables

To understand the nonlinear evolution in terms of normal modes of MHD, we adopt the decomposition of the fluctuations into characteristic variables. In an isothermal system, wave dissipation does not increase the temperature (and the speed of sound); consequently the background (mean) field is always steady and uniform, and the mean and fluctuation of each variable are easily decoupled.

In terms of primitive variables $\mathbf{W}^T = (\rho, v_x, v_y, B_y)$, the governing equations, Eqs.

(2) – (5), can be rewritten as

$$\frac{\partial}{\partial t} \mathbf{W} + \mathbf{A}(\mathbf{W}) \cdot \frac{\partial}{\partial x} \mathbf{W} = 0, \quad (9)$$

where $\mathbf{A}(\mathbf{W})$ is the characteristic matrix of the primitive variables, explicitly written as

$$\mathbf{A}(\mathbf{W}) = \begin{pmatrix} v_x & \rho & 0 & 0 \\ C_s^2/\rho & v_x & 0 & B_y/\rho \\ 0 & 0 & v_x & -B_0/\rho \\ 0 & B_y & -B_0 & v_x \end{pmatrix}. \quad (10)$$

Following Stone et al. (2008), the right and left eigenmatrices of $\mathbf{A}(\mathbf{W})$ are explicitly given as

$$\mathbf{R}(\mathbf{W}) = \begin{pmatrix} \rho\alpha_f & \rho\alpha_s & \rho\alpha_s & \rho\alpha_f \\ -C_{ff} & -C_{ss} & C_{ss} & C_{ff} \\ C_{ss} & -C_{ff} & C_{ff} & -C_{ss} \\ A_s & -A_f & -A_f & A_s \end{pmatrix}, \quad (11)$$

and

$$\mathbf{L}(\mathbf{W}) = \begin{pmatrix} \alpha_f/2\rho & -C_{ff}/2C_s^2 & C_{ss}/2C_s^2 & A_s/2\rho C_s^2 \\ \alpha_s/2\rho & -C_{ss}/2C_s^2 & -C_{ff}/2C_s^2 & -A_f/2\rho C_s^2 \\ \alpha_s/2\rho & C_{ss}/2C_s^2 & C_{ff}/2C_s^2 & -A_f/2\rho C_s^2 \\ \alpha_f/2\rho & C_{ff}/2C_s^2 & -C_{ss}/2C_s^2 & A_s/2\rho C_s^2 \end{pmatrix}, \quad (12)$$

where each variable is a function of the local fast and slow mode velocities C_{fast} and C_{slow} , respectively:

$$C_{fast}^2 = \frac{1}{2} \left[C_s^2 + \frac{B_0^2 + B_y^2}{4\pi\rho} + \sqrt{\left(C_s^2 + \frac{B_0^2 + B_y^2}{4\pi\rho} \right)^2 - 4C_s^2 \frac{B_0^2}{4\pi\rho}} \right],$$

$$C_{slow}^2 = \frac{1}{2} \left[C_s^2 + \frac{B_0^2 + B_y^2}{4\pi\rho} - \sqrt{\left(C_s^2 + \frac{B_0^2 + B_y^2}{4\pi\rho} \right)^2 - 4C_s^2 \frac{B_0^2}{4\pi\rho}} \right],$$

$$\alpha_f = \frac{C_s^2 - C_{slow}^2}{C_{fast}^2 - C_{slow}^2}, \quad \alpha_s = \frac{C_{fast}^2 - C_s^2}{C_{fast}^2 - C_{slow}^2},$$

$$C_{ff} = C_{fast}\alpha_f, \quad C_{ss} = C_{slow}\alpha_s,$$

$$A_f = C_s\alpha_f\sqrt{\rho} \quad \text{and} \quad A_s = C_s\alpha_s\sqrt{\rho}.$$

The mean field \mathbf{W}_0 is trivial:

$$\mathbf{W}_0 = \begin{pmatrix} \rho_0 \\ 0 \\ 0 \\ 0 \end{pmatrix}, \quad (13)$$

and the fluctuation field can easily be obtained by subtracting \mathbf{W}_0 from \mathbf{W} as $\Delta\mathbf{W} = \mathbf{W} - \mathbf{W}_0$. The fluctuation can then be decomposed via “the local” right eigenmatrix $\mathbf{R}(\mathbf{W})$ ($\neq \mathbf{R}(\mathbf{W}_0)$) as

$$\Delta\mathbf{W} = \mathbf{R}(\mathbf{W}) \cdot \boldsymbol{\alpha}(\mathbf{W}) \quad (14)$$

or more explicitly,

$$\begin{pmatrix} \Delta\rho \\ \Delta v_x \\ \Delta v_y \\ \Delta B_y \end{pmatrix} = \begin{pmatrix} \rho\alpha_f & \rho\alpha_s & \rho\alpha_s & \rho\alpha_f \\ -C_{ff} & -C_{ss} & C_{ss} & C_{ff} \\ C_{ss} & -C_{ff} & C_{ff} & -C_{ss} \\ A_s & -A_f & -A_f & A_s \end{pmatrix} \begin{pmatrix} \alpha_{fl} \\ \alpha_{sl} \\ \alpha_{sr} \\ \alpha_{fr} \end{pmatrix}, \quad (15)$$

where $\boldsymbol{\alpha}$ is a vector of amplitudes. In terms of $\boldsymbol{\alpha}$, this equation can be solved as

$$\boldsymbol{\alpha}(\mathbf{W}) = \mathbf{L}(\mathbf{W}) \cdot \Delta\mathbf{W}. \quad (16)$$

Each column of matrix \mathbf{R} corresponds to a right eigenvector of \mathbf{A} : $\boldsymbol{\psi}_i$. Therefore, we can rewrite \mathbf{R} as $\mathbf{R} = (\boldsymbol{\psi}_{fl}, \boldsymbol{\psi}_{sl}, \boldsymbol{\psi}_{sr}, \boldsymbol{\psi}_{fr})$. The fluctuation of mode i , $\Delta\mathbf{W}_i$ is the following product of α_i and $\boldsymbol{\psi}_i$

$$\Delta\mathbf{W}_i = \alpha_i \boldsymbol{\psi}_i \quad (i = fl, sl, sr, fr) \quad (17)$$

where fl and sl denote leftward Alfvén and acoustic waves, respectively, and sr and fr denote the corresponding rightward waves.

3. Results

3.1. Time evolutions of density, velocity and magnetic field

3.1.1. Evolutions of raw data

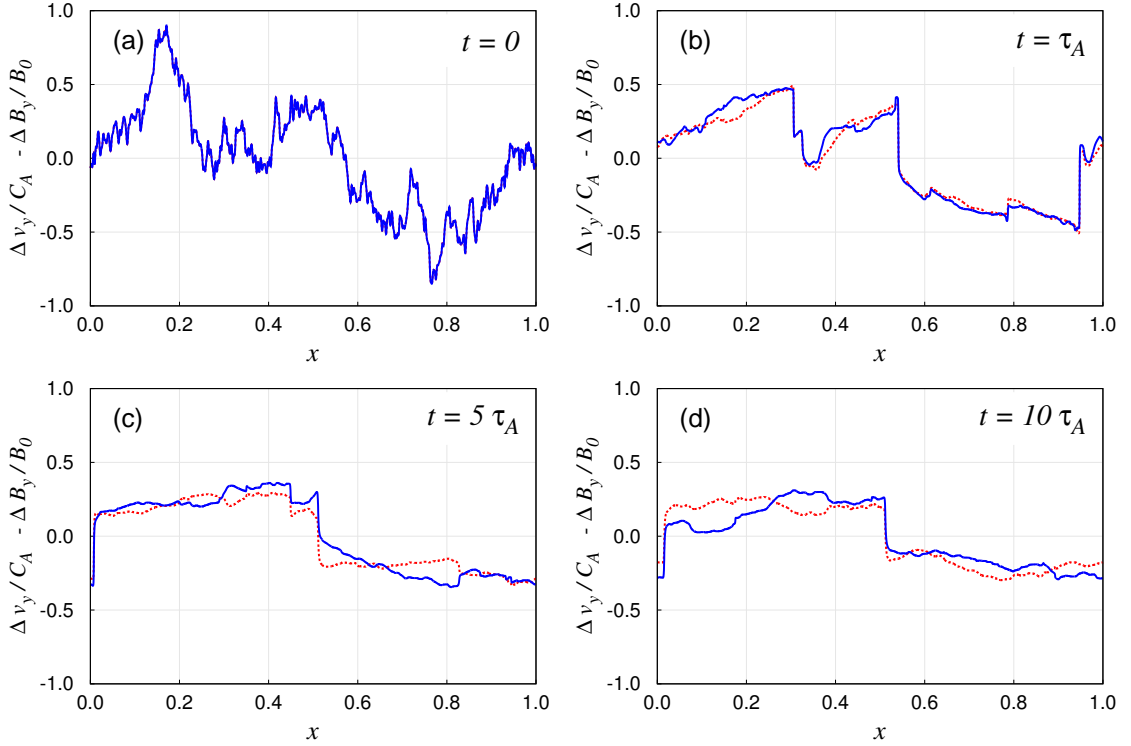


Fig. 1.— Snapshots of $\Delta v_y/C_A$ (blue, solid line) and $-\Delta B_y/B_0$ (red, dotted line) in typical case ($E_{wave}/E_{gas} = 0.5$ $C_s/C_A = 0.5$). Snapshots are captured at (a) $t = 0$, (b) $t = \tau_A$, (c) $t = 5\tau_A$ and (d) $t = 10\tau_A$.

Figures 1 and 2 show the time evolutions of normalized physical quantities in a typical case in which the initial wave energy E_{wave} equals one-half of the background thermal energy E_{gas} :

$$E_{gas} = \rho_0 C_s^2 L, \quad (18)$$

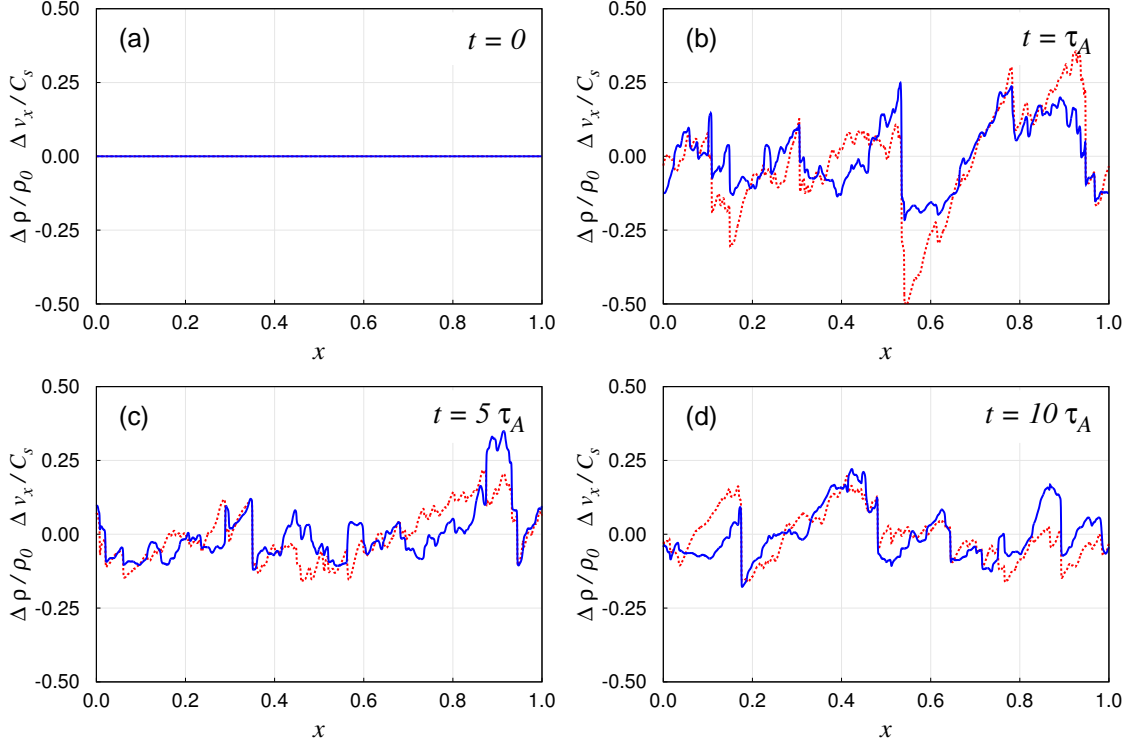


Fig. 2.— Snapshots of $\Delta \rho / \rho_0$ (blue, solid line) and $\Delta v_x / C_s$ (red, dotted line). Parameters and evolution times are those of Fig. 1.

The background plasma beta is set to $\beta = 0.25$ ($C_s / C_A = 0.5$). Fig. 1 presents the evolutions of transverse fluctuations Δv_y , ΔB_y . Steepening of the magnetic field is seen, which has been analytically explained by Montgomery (1959), Cohen & Kulsrud (1974) and Kennel et al. (1990). The decreased number of shock fronts results not only from dissipation but also from the merging of shocks. In other words, when two fast shock waves collide, they merge into a stronger fast shock. In this case, a few strong shocks successively overtake many weak shocks and merge with them, reducing their number. This apparent inverse cascade should not be interpreted as the energy transport toward large scales. The deviation of $\Delta v_y / C_A$ from $-\Delta B_y / B_0$ in Fig. 1 confirms that reflection occurs

in our simulation, because it shows that the nonzero component of the normalized leftward Elsässer variable $z^- = \Delta v_y/C_A + \Delta B_y/B_0$ exists.

Fig. 2 reveals many slow (acoustic) shock waves generated by the magnetic pressure of wave. This effect is called nonlinear mode conversion from Alfvén waves to acoustic waves (Hollweg et al. 1982; Kudoh & Shibata 1999; Moriyasu et al. 2004; Suzuki & Inutsuka 2005). Unlike in the transverse field, the number of shock fronts does not evidently decrease even at $t = 10\tau_A$. There are several reasons for this. First is the long overtaking time of the slow shock waves caused by the small speed of sound (in the present low-beta case). Second, the shock formations occur at different time scales. The formation times of fast and slow shock waves are inversely proportional to the square of the nonlinearity and the nonlinearity itself, respectively. That is, denoting the shock formation times of fast and slow waves by τ_f and τ_s , respectively, we have

$$\tau_f \propto \left(\frac{\Delta v_y}{C_A}\right)^{-2} \quad \tau_s \propto \left(\frac{\Delta v_x}{C_s}\right)^{-1}. \quad (19)$$

Since the relation $\Delta v_x/C_s \sim \Delta v_y/C_A < 1$ is generally satisfied in our calculation, slow shock waves are more easily generated than fast shock waves. Third, new acoustic waves are continuously generated by the magnetic pressure of the Alfvén waves. Despite the shock dissipation, the amplitude decreases less markedly than in transverse fields, which supports the third reason

We also perform the simulations with initially monochromatic wave with a wavelength of the box size L . Although there are several differences, the evolutions were similar with the red-noise case, especially for the transverse fields. This is because the red-noise wave has the largest energy in the longest-wavelength mode.

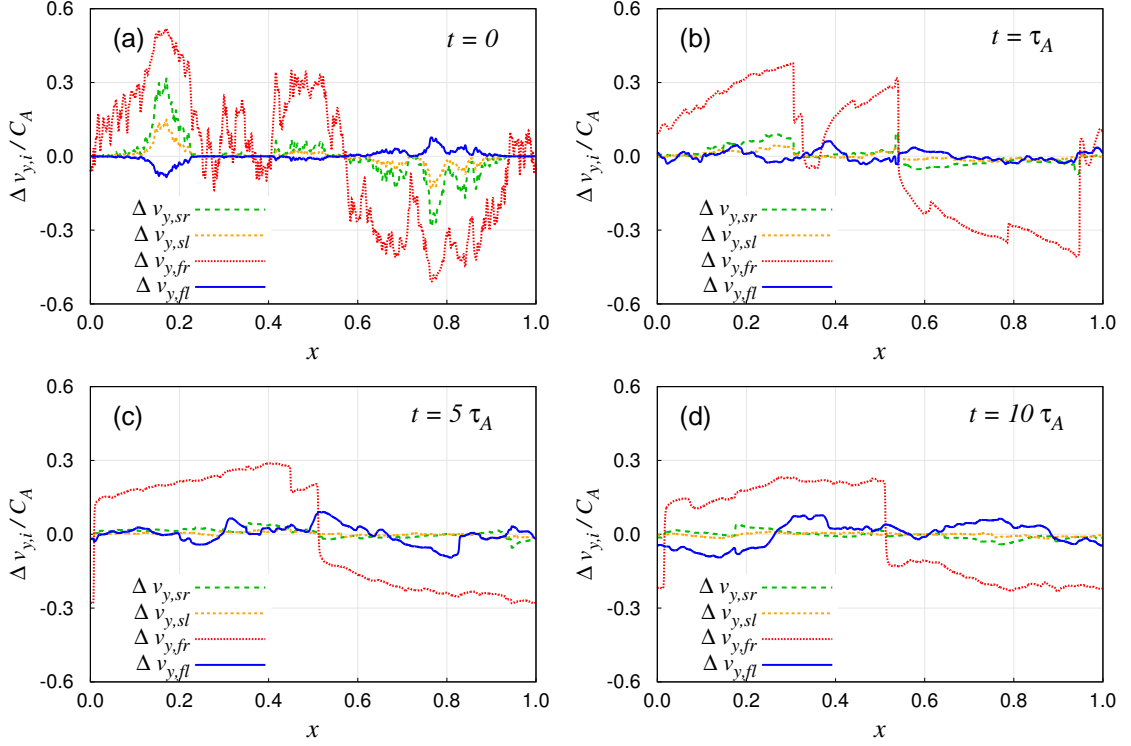


Fig. 3.— Results of decomposed fluctuation $\Delta v_{y,i}$. Four lines correspond to modes $\Delta v_{y,fr}$ (red, dotted line), $\Delta v_{y,fl}$ (blue, solid line), $\Delta v_{y,sr}$ (green, long-dashed line) and $\Delta v_{y,sl}$ (orange, short-dashed line).

3.1.2. Evolutions of decomposed data

Figures 3 and 4 show the evolutions in the typical case of the decomposed fluctuations $\Delta v_{y,i}$ and $\Delta v_{x,i}$ (where i represents a mode) defined in Section 2.3. Although we initially impose a purely rightward Elsässer state, not only a rightward Alfvénic fluctuation $\Delta v_{y,fr}$, but also those of other modes, $\Delta v_{y,fl}$, $\Delta v_{y,sr}$, $\Delta v_{y,sl}$ appear (Fig. 3). This contamination originates from the finite-amplitude effect, which deviates the Elsässer variables from the fast-mode characteristics. The most important feature in this figure is the increase of the amplitude of $\Delta v_{y,fl}$ from $t = 0$ to $t = 10\tau_A$, which provides direct evidence of reflection.

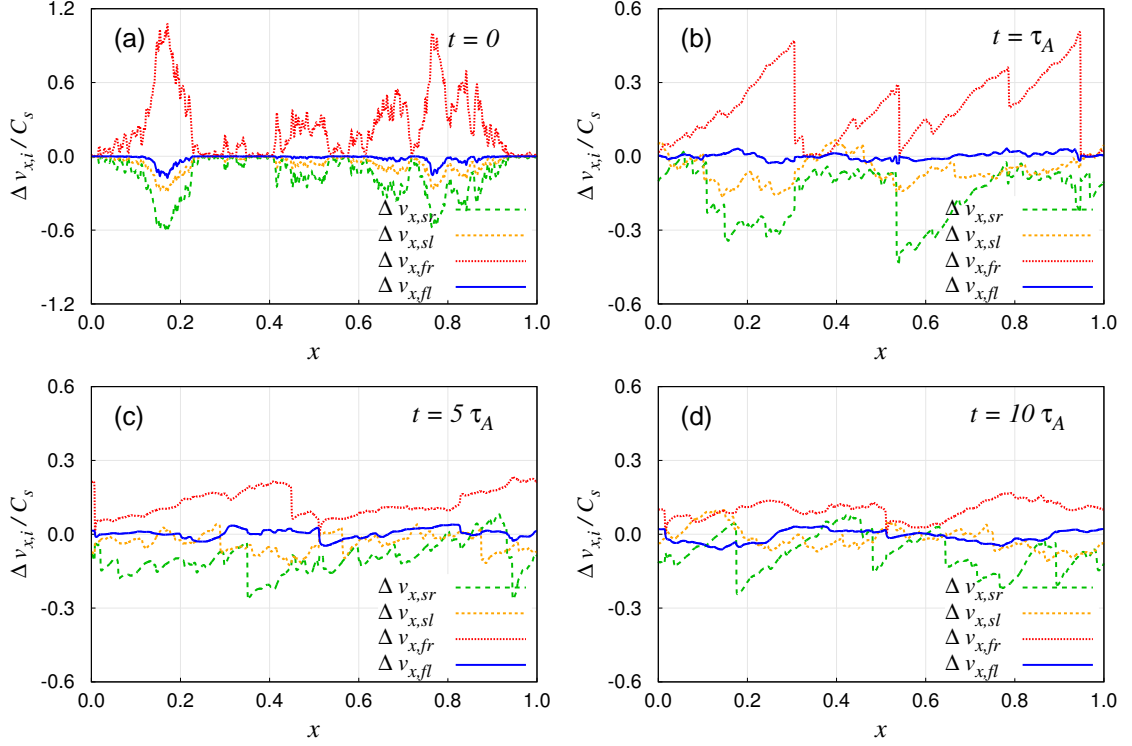


Fig. 4.— Results of decomposed fluctuation $\Delta v_{x,i}$. Four lines correspond to modes $\Delta v_{x,fr}$ (red, dotted line), $\Delta v_{x,fl}$ (blue, solid line), $\Delta v_{x,sr}$ (green, long-dashed line) and $\Delta v_{x,sl}$ (orange, short-dashed line). Vertical axis scale differs between (a) and (b).

Fig. 4 shows the behavior of the longitudinal fluctuations. It is initially transported by the rightward Alfvén wave. However, the amplitude of Δv_x gradually shifts from the rightward Alfvén wave to the rightward acoustic (slow) wave. This shift occurs probably because nonlinear interactions of Alfvén waves decrease the nonlinearity of the Alfvén waves and generate acoustic waves.

3.2. Self-energy evolution

3.2.1. Short-term behavior

In this subsection, we discuss the physical mechanism of wave reflection. For this purpose, we examine the evolutions of the individual modes. In terms of the decomposed density $\Delta\rho_i$, velocities $\Delta v_{x,i}$ and $\Delta v_{y,i}$, and the magnetic field $\Delta B_{y,i}$, the normalized “self-energy” of each wave mode i can be defined as

$$E_i = \int_0^L dx \left[\frac{1}{2} (\rho_0 + \Delta\rho_i) (\Delta v_{x,i}^2 + \Delta v_{y,i}^2) + \frac{\Delta B_{y,i}^2}{8\pi} \right] / E_{wave} \quad (i = fl, sl, sr, fr). \quad (20)$$

Note that the summation of E_i over modes i does not agree with the total energy of the fluctuations because it excludes the interaction terms between two modes.

Figure 5 shows the evolving self-energies in the typical case ($E_{wave}/E_{gas} = 0.5$, $C_s/C_A = 0.5$). Quasi-periodic energy oscillations are evident in each mode. In particular, the phases of the leftward Alfvén wave energy E_{fl} and leftward acoustic wave energy E_{sl} are negatively correlated. This phase-anticorrelated oscillation suggests the exchange of energy via resonance between these two modes. Other simulation runs, in which we changed E_{wave}/E_{gas} and C_s/C_A (results not shown), confirm that phase-anticorrelated oscillations always appear except such cases with high wave energy ($E_{wave} > E_{gas}$) and extremely low plasma beta.

Figure 6 shows the results of a case with the low plasma beta and the large amplitude ($C_s/C_A = 0.1$ and $E_{wave}/E_{gas} = 2$). We have found that the decay instability appears. This finding is important, as it confirms the possibility of decay instability in linearly polarized waves. The extremely-low beta condition is essential, because decay instability never occurs when $C_s/C_A = 0.5$. Note that the evolutions of self-energies (especially of the leftward Alfvén wave) in Fig. 6 differs from those in Fig. 5, indicating that the physical process commonly observed in our simulations differs from the usual decay instability. E_{fl} increases

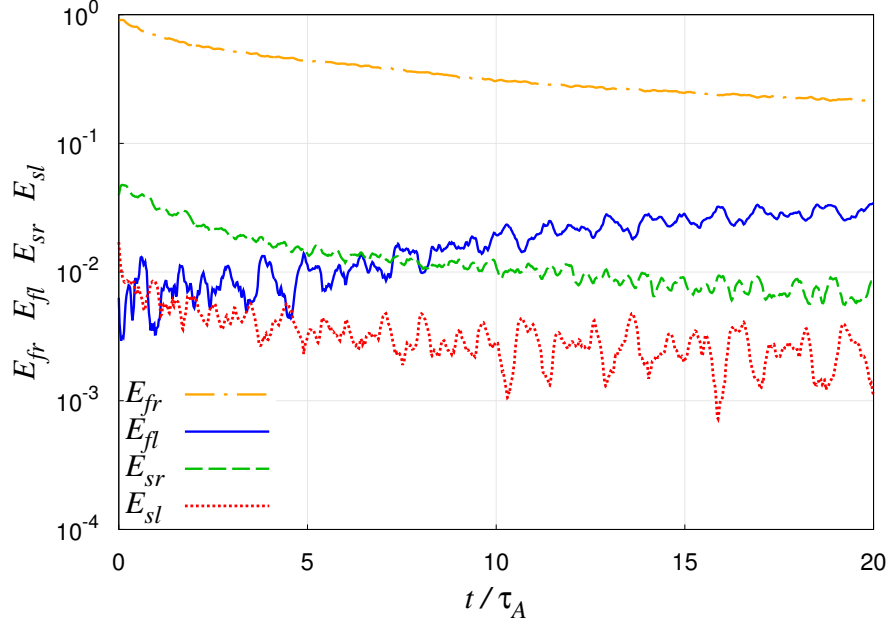


Fig. 5.— Time evolutions of self-energies in the typical case ($E_{wave}/E_{gas} = 0.5$ and $C_s/C_A = 0.5$). Four lines represent rightward Alfvén wave energy E_{fr} (orange, dash-dotted line), leftward Alfvén wave energy E_{fl} (blue, solid line), rightward acoustic wave energy E_{sr} (green, dashed line), and leftward acoustic wave energy E_{sl} (red, dotted line).

almost exponentially between $t = \tau_A$ and $t = 4\tau_A$, providing direct evidence of some instability. Since this is an instability of Alfvén waves in low-beta plasmas, it is definitely the decay instability. E_{fl} saturates at values comparable to E_{fr} , when the feedback process is no longer negligible. This feedback appears in Fig. 6 after $t = 5\tau_A$, when E_{fr} increases by the feedback from the leftward Alfvén waves.

To examine the wave energy oscillation and correlation between two modes in detail,

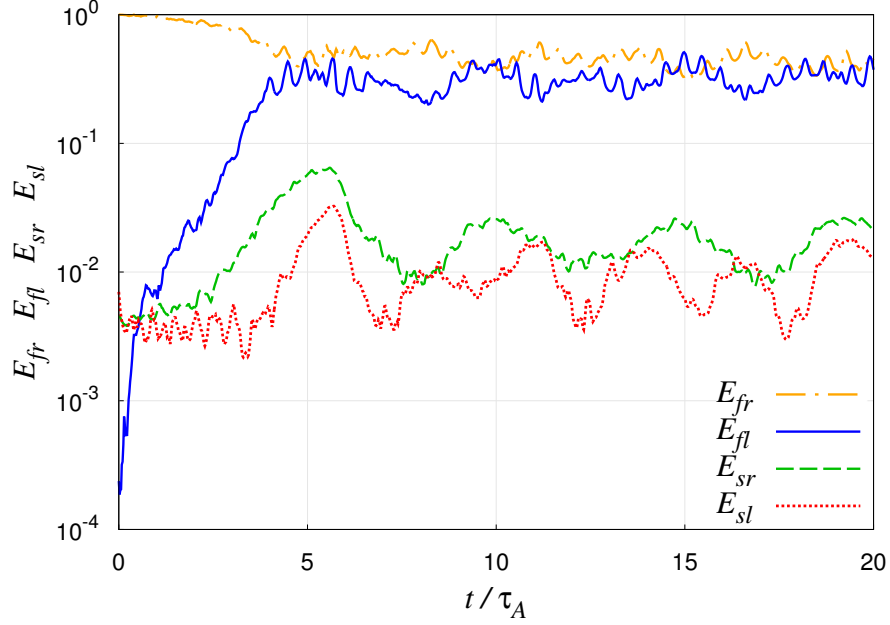


Fig. 6.— Decay instability case. Parameters are set to $C_s/C_A = 0.1$ and $E_{wave}/E_{gas} = 2$.

we average each E_i over time. The averaged energy here is defined as

$$\overline{E}_i(t) = \sqrt[2N_A+1]{\prod_{j=-N_A}^{N_A} E_i(t+j\Delta t)}, \quad (21)$$

where Δt is the cadence of the data and $N_A\Delta t$ is the Alfvén time ($N_A = \tau_A/\Delta t$). The fluctuation part ΔE_i is defined in terms of \overline{E}_i as

$$\Delta E_i = E_i - \overline{E}_i. \quad (22)$$

To illustrate the dominant correlation between the leftward Alfvén and acoustic modes, we generate scatter plots between the energy fluctuations of different modes ΔE_i and ΔE_j and computed the correlation factors C . Both of them reveal the strongest correlation between ΔE_{fl} and ΔE_{sl} among combinations of the modes. From these facts we inferred the successive exchange of energy, mainly between the leftward Alfvén and acoustic waves.

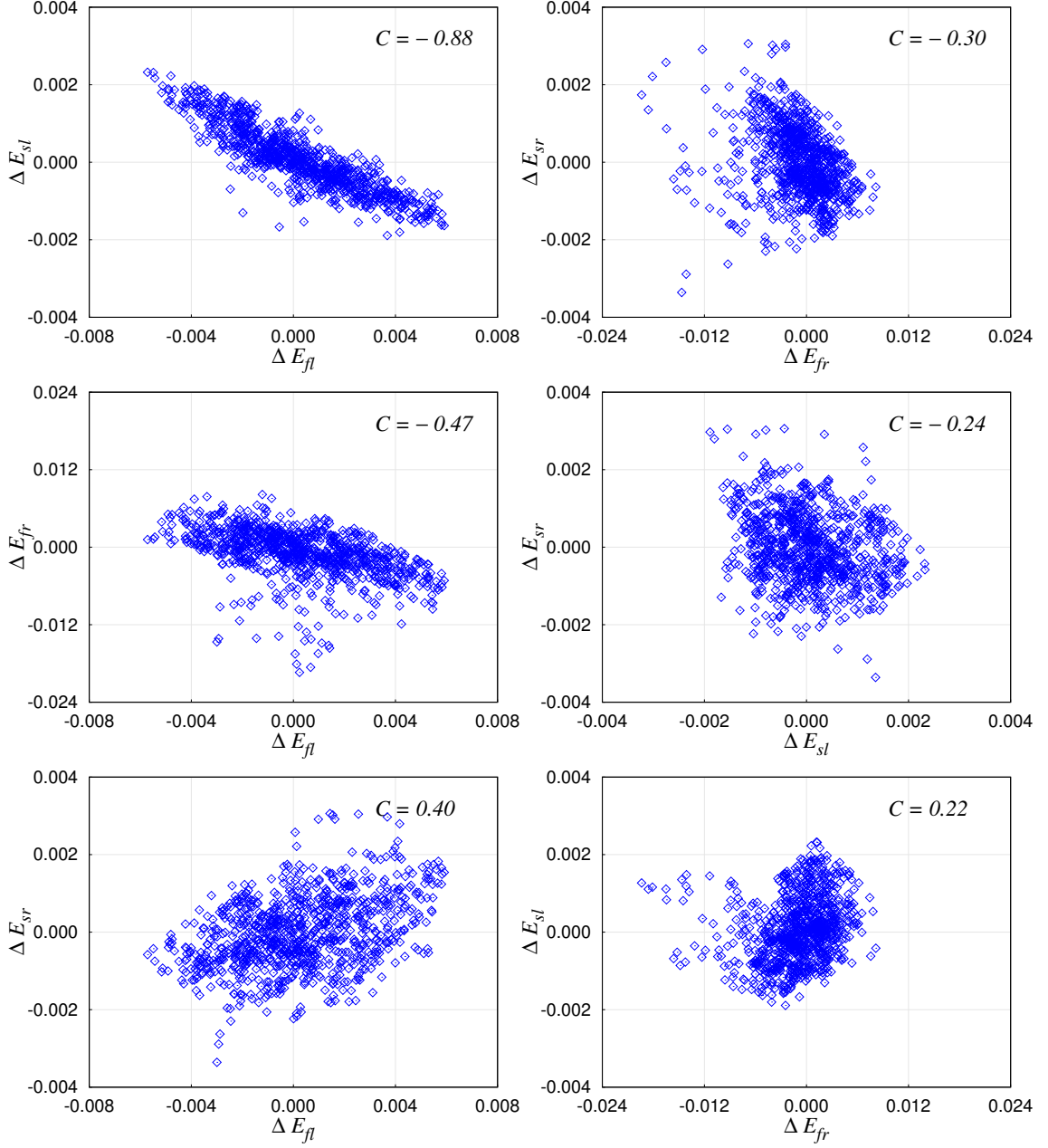


Fig. 7.— Scatter plots for all ΔE_i and ΔE_j . Correlation factor C of each set is displayed inside corresponding panel. As demonstrated by plot profiles and C values, strongest correlation occurs between ΔE_{fl} and ΔE_{sl} . We have confirmed this result in other parameter sets.

3.2.2. Long-term behavior

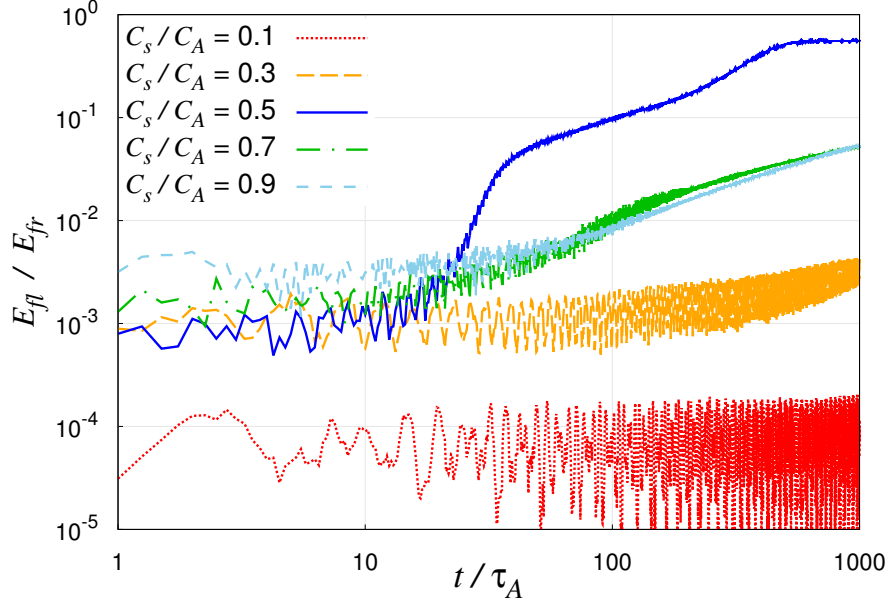


Fig. 8.— Evolutions of population ratio with same energy ratio ($E_{wave}/E_{gas} = 0.25$) and different plasma betas $C_s/C_A = 0.1$ (red, dotted line), 0.3 (orange, long-dashed line), 0.5 (blue, solid line), 0.7 (green, dash-dotted line), 0.9 (light-blue, short-dashed line).

We now present the long-term evolution of the system, up to $t = 1000\tau_A$. In particular, we focus on the population ratio (or reflection ratio) defined as E_{fl}/E_{fr} . In Fig. 8, it is shown for cases with $C_s/C_A = 0.1, 0.3, 0.5, 0.7$, or 0.9 , fixing $E_{wave}/E_{gas} = 0.25$. When $C_s/C_A = 0.5$, the population ratio is anomalously rapidly enhanced around $t = 20\tau_A$. This efficient reflection is an essentially nonlinear phenomenon that amplifies the growth rate over time. When the initial energy of the fluctuations equals the thermal energy of the background, that is, when $E_{wave} = E_{gas}$, fast reflections occur not only when $C_s/C_A = 0.5$ but also when $C_s/C_A = 0.7$ and $C_s/C_A = 0.9$. The increased nonlinearity permits rapid

enhancement of the population ratio over wider parameter space, because sufficient energy is available for the reflection. Such rapid enhancement also supports that the wave resonance is critical, because the timescale of the resonance decreases with increasing amplitude of the coupled waves.

4. Discussion

4.1. Physical process of reflection

In the previous section, we demonstrate two enhancement features of E_{fl} and E_{fl}/E_{fr} .

1. Nonmonotonic increase of the leftward Alfvén wave energy E_{fl} , which involves short-period oscillations anti-correlated with the leftward acoustic wave energy E_{sl} .
2. Nonconstant (initially increasing) growth of the population ratio E_{fl}/E_{fr} . The temporal evolution of E_{fl}/E_{fr} is nonmonotonically sensitive to the β value. In particular, when $C_s/C_A = 0.5$, the population ratio is enhanced at an anomalous rate, as shown in Fig. 8.

In this section, we discuss theoretically an elementary reflection process that explains above features. We focus on the typical case ($E_{wave}/E_{gas} = 0.5, C_s/C_A = 0.5$) here. To clarify the physical process of the reflection, we perform Fourier transformation in space to the normalized velocity fluctuation $\Delta v_{y,fr}$, $\Delta v_{y,fl}$, $\Delta v_{x,sr}$ and $\Delta v_{x,sl}$. Notice that normalization factors are different between fast (Alfvén) and slow (acoustic) modes. We refer to each Fourier mode by the wavenumber normalized by $2\pi/L$, that is, mode p represents a mode whose wavenumber is $2\pi p/L$ (wave length is L/p). Due to the periodic boundary condition, p is limited to integers.

First, we focus on feature 1, i.e., phase-anticorrelated energy oscillations between two

leftward waves. Resonance between these two waves can naturally explain this behavior, that is, interaction between some parent and leftward Alfvén waves generates a leftward acoustic mode via three-wave resonance and similarly, interaction between some parent and a leftward acoustic waves generates a leftward Alfvén wave. This is a stable process because, since the wave momenta should be conserved during wave-wave interactions, leftward Alfvén and acoustic waves cannot amplify their energies at the same time but just oscillate their energies. Rightward Alfvén waves can be a parent wave (i.e., energy mediator) in this process, because, different from the decay instability, three-wave resonance with a forward Alfvén wave as a parent wave and backward Alfvén and acoustic waves as daughter waves is a stable process. This resonant energy exchange may play an important role in the saturation of E_{fl} , because E_{fl} is likely to be transported to E_{sl} , which is much easier to dissipate via the shock wave dissipation than E_{fl} .

Next, we discuss on the amplification process of E_{fl} . In Figure 9, we show the Fourier-transformed amplitudes of $\Delta v_{y,fr}$ and $\Delta v_{y,fl}$. In the left panel of Fig. 9, where rightward Alfvén wave is focused, we show the temporal evolutions of modes 2 to 5. Although all modes decrease their amplitudes initially, odd-number modes recover their amplitude. This is caused by the steepening of mode 1: It generates density fluctuations (not acoustic waves) of mode 2 via the magnetic pressure and cascades (steepens) by interacting with the density fluctuations. Interaction between mode 1 Alfvén wave and mode 2 density fluctuation generates mode 3 Alfvén wave, which as well generates mode 5 Alfvén wave by the interaction with the density fluctuation. In this way, only odd-number modes survive.

After the steepening, lower-number modes tend to have higher amplitudes, which is not the case in Fig. 9 after $t = 17\tau_A$. This behavior indicates some energy absorption from mode 3 rightward Alfvén wave. In the right panel of Fig. 9 we show the leftward

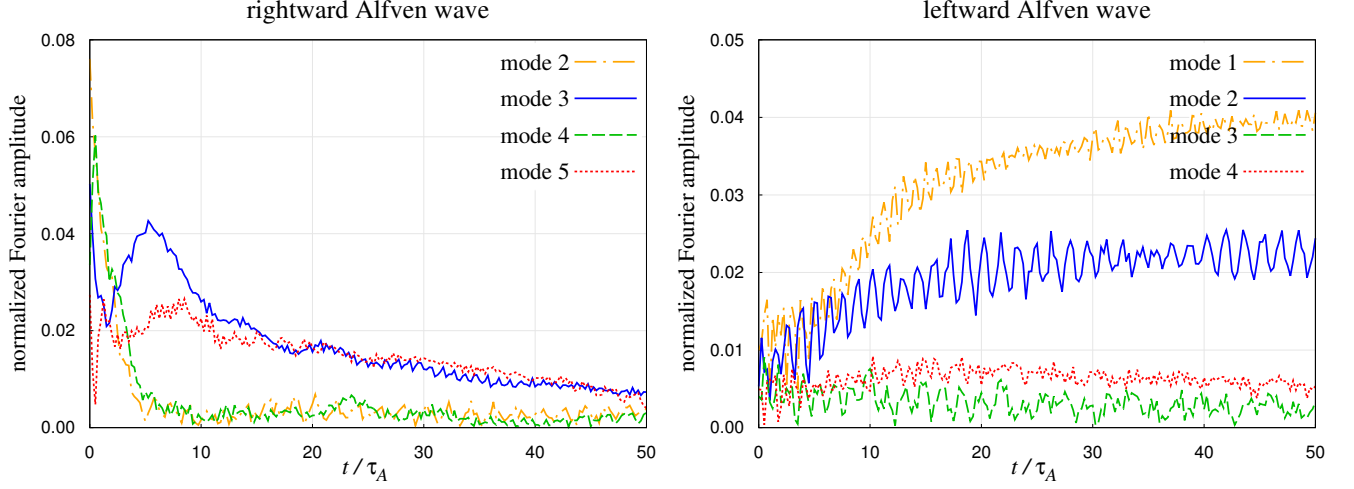


Fig. 9.— Time evolutions of the Fourier amplitudes of $\Delta v_{y,fr}/C_A$ and $\Delta v_{y,fl}/C_A$ the for typical case ($E_{wave}/E_{gas} = 0.5, C_s/C_A = 0.5$). Left panel shows the evolutions of mode 2 (orange, dash-dotted line), mode 3 (blue, solid line), mode 4 (green, dashed line) and mode 5 (red, dotted line) of rightward Alfvén waves, while right panel shows those of mode 1 (orange, dash-dotted line), mode 2 (blue, solid line), mode 3 (green, dashed line) and mode 4 (red, dotted line) of leftward Alfvén waves, respectively.

Alfvén waves of modes 1 to 4. The dominant mode of the reflected Alfvén wave is mode 1. Considering the possibility of some energy absorption from mode 3 rightward Alfvén wave, the decay instability is the promising process of the amplification, because mode 3 rightward Alfvén and mode 1 leftward Alfvén waves can satisfy the three-wave resonance condition of the decay instability in this plasma beta ($C_s/C_A = 0.5$). This is explained as follows. The three-wave resonance condition of the decay instability is given as

$$\begin{pmatrix} k_0 \\ \omega_0 \end{pmatrix} = \begin{pmatrix} -k_1 \\ \omega_1 \end{pmatrix} + \begin{pmatrix} k_2 \\ \omega_2 \end{pmatrix} \quad (23)$$

$$\omega_0 = k_0 C_A \quad \omega_1 = -k_1 C_A \quad \omega_2 = k_2 C_s,$$

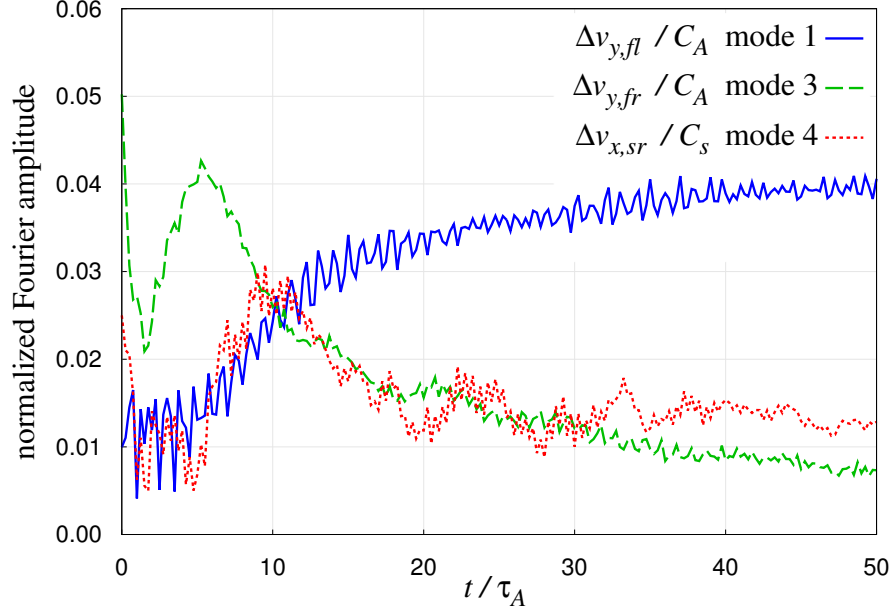


Fig. 10.— Evidence of the decay instability. Each line shows the velocity amplitude of mode 1 leftward Alfvén wave (blue, solid line), mode 3 rightward Alfvén wave (green, dashed line) and mode 4 rightward acoustic wave (red, dotted line).

where k_0 , k_1 and k_2 are wavenumbers of the rightward Alfvén (parent), leftward Alfvén and rightward acoustic waves, respectively. After solving this, we obtain following relation.

$$(k_0 : k_1 : k_2) = \left(1 + \frac{C_s}{C_A} : 1 - \frac{C_s}{C_A} : 2 \right). \quad (24)$$

By substituting $C_s/C_A = 0.5$, it is shown that mode 1 leftward Alfvén wave can absorb the energy of mode 3 rightward Alfvén wave via the decay instability with mode 4 rightward acoustic wave another daughter wave. To support this, we show in Figure 10 Fourier-transformed velocity amplitudes of these three modes, that is, mode 3 rightward Alfvén, mode 1 leftward Alfvén and mode 4 rightward acoustic waves. It is clear that leftward Alfvén and rightward acoustic waves increase their energy at the same time as

the rightward Alfvén wave decays. We have confirmed that the energy increase of mode 4 rightward acoustic wave is not by the steepening, because it exceeds energies of the other modes when it reaches its maximum. If circularly polarized, mode 1 Alfvén waves never steepen but decay directly to mode 1 backscattered Alfvén waves, which is the usual process of the decay instability. This difference shows that linear polarization and resultant steepening generate a new energy channels, which is effective at least in the typical case. In Figure 11, we summarize these new-found elementary processes and energy channels by a schematic diagram.

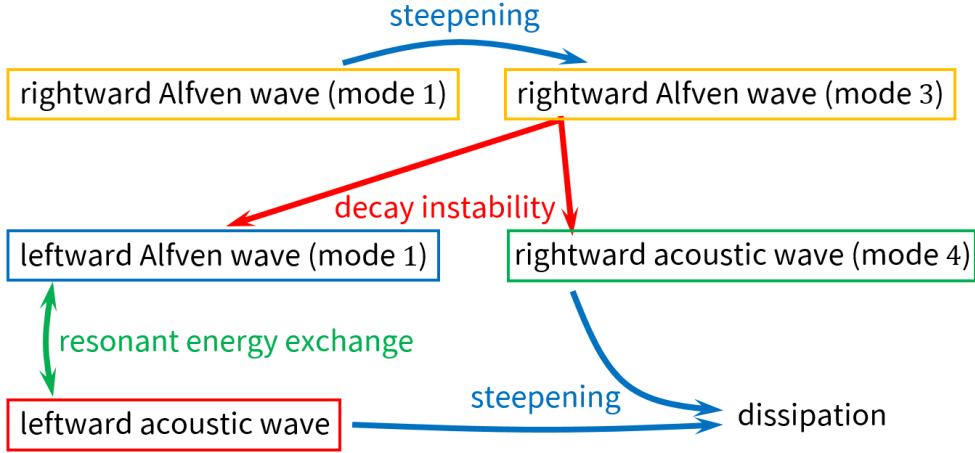


Fig. 11.— Schematic diagram of the energy channels found in the typical case.

4.2. Application to open system

In this subsection, we present the comparison of our results on the population ratio E_{fl}/E_{fr} with solar wind observations. Because the plasma beta in the solar wind changes with distance, some technical interpretation is necessary. Our results and the observational data are not directly comparable. Instead, we average our results for various plasma betas. Specifically, we calculate five cases ($C_s/C_A = 0.5, 0.6, 0.7, 0.8, 0.9$) with fixed the

initial energy ratio $E_{wave}/E_{gas} = 1$, which is observationally appropriate according to Goldstein et al. (1995). We then average the results by using Eq. (25). Here $R(t; \alpha)$ and $\overline{R}(t)$ denote the time evolution of E_{fl}/E_{fr} with $C_s/C_A = \alpha$ and the averaged result, respectively.

$$\overline{R}(t) = \frac{1}{5} [R(t; 0.5) + R(t; 0.6) + R(t; 0.7) + R(t; 0.8) + R(t; 0.9)]. \quad (25)$$

Next we convert time in our results to the distance in real solar wind. We use

$$r - r_{0.1} = V_{SW}(t - t_{0.1}) \quad (26)$$

in this conversion, where V_{SW} is the solar wind speed assumed as 750 km/sec, r is the radius from the sun center, $t_{0.1}$ is the time at which $E_{fl}/E_{fr}=0.1$ in our results, and $r_{0.1}$ is the location at which $\overline{R}(t) = 0.1$ in the fast solar wind observations. According to Goldstein et al. (1995), $r_{0.1} = 1$ AU. The time on the right hand side of Eq. (26) is normalized by the Alfvén time τ_A , assigned as the dominant wave period in the solar wind fluctuations, i.e., 10^4 sec. This value is determined from the dominant frequency (10^{-4} Hz) in the measured fast solar wind fluctuations (Tu & Marsch 1995). The obtained $\overline{R}(r)$ are compared with the observational values of Bavassano et al. (2000) in Figure 12. Our results favorably agree with the observations. To our knowledge, these trends have been best explained by linear reflection (Verdini & Velli 2007) and decay instability (Del Zanna et al. 2001). However, the linear reflection process requires the most dominant frequency of Alfvén waves to be 10^{-6} Hz. At Alfvén wave frequencies around 10^{-4} Hz, linear reflection cannot generate sufficient reflected waves enough (Cranmer & van Ballegooijen 2005). On the other hand, decay instability cannot explain the saturation of E_{fl}/E_{fr} around 0.5 beyond 3 AU. Our results (Fig. 12) explain the observations while alleviating both difficulties.

There are several points to improve which are simplified in this study. First, since our system is periodic in space, we need to confirm that our proposed process operates

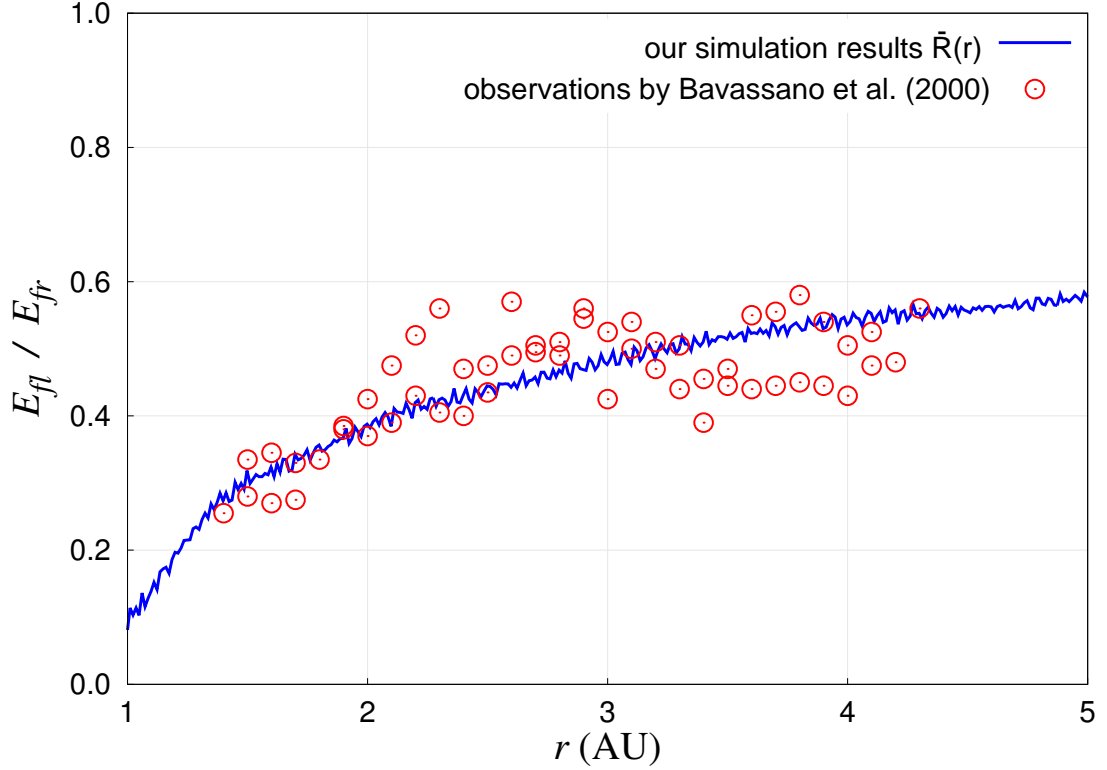


Fig. 12.— Energy ratios of leftward and rightward propagating Alfvén waves: Continuous curve and open circles denote our simulation results (\bar{R} , see text for details), and observations by Bavassano et al. (2000), respectively.

in open systems. Second, we should consider kinetic effects in the solar wind condition; most critically, Landau damping of (ion-)acoustic waves. When the Landau damping is too strong, the acoustic waves dissipate before the backscattering via the decay instability. Third, one-dimensional uniform-background simulations usually overestimate the shock effects and neglect the expansion effect of the solar wind (Grappin et al. 1993; Nariyuki 2015; Del Zanna et al. 2015). For an investigation of this influence, it requires multidimensional simulations.

The authors acknowledge Takeru K. Suzuki and Takuma Matsumoto for their fruitful discussions. One of the authors (M. Shoda) also thanks Masahiro Hoshino for his discussions and critical advice. This research is supported by Leading Graduate Course for Frontiers of Mathematical Sciences and Physics (FMSP) and JSPS KAKENHI Grant Number 15H03640.

REFERENCES

- An, C.-H., Suess, S. T., Moore, R. L., & Musielak, Z. E. 1990, *ApJ*, 350, 309
- Antolin, P., Shibata, K., Kudoh, T., Shiota, D., & Brooks, D. 2008, *ApJ*, 688, 669
- Bavassano, B., Pietropaolo, E., & Bruno, R. 2000, *J. Geophys. Res.*, 105, 15959
- Belcher, J. W. 1971, *ApJ*, 168, 509
- Belcher, J. W., & Davis, Jr., L. 1971, *J. Geophys. Res.*, 76, 3534
- Chandran, B. D. G., Quataert, E., Howes, G. G., Hollweg, J. V., & Dorland, W. 2009, *ApJ*, 701, 652
- Cohen, R. H., & Kulsrud, R. M. 1974, *Physics of Fluids*, 17, 2215
- Cranmer, S. R., & van Ballegooijen, A. A. 2005, *ApJS*, 156, 265
- Cranmer, S. R., van Ballegooijen, A. A., & Edgar, R. J. 2007, *ApJS*, 171, 520
- De Pontieu, B., et al. 2007, *Science*, 318, 1574
- Del Zanna, L., Matteini, L., Landi, S., Verdini, A., & Velli, M. 2015, *Journal of Plasma Physics*, 81, 013202
- Del Zanna, L., Velli, M., & Londrillo, P. 2001, *A&A*, 367, 705
- Dewar, R. L. 1970, *Physics of Fluids*, 13, 2710
- Dmitruk, P., Matthaeus, W. H., Milano, L. J., Oughton, S., Zank, G. P., & Mullan, D. J. 2002, *ApJ*, 575, 571
- Dobrowolny, M., Mangeney, A., & Veltri, P. 1980, *Physical Review Letters*, 45, 144
- Ferraro, C. A., & Plumpton, C. 1958, *ApJ*, 127, 459

- Fujimura, D., & Tsuneta, S. 2009, *ApJ*, 702, 1443
- Fukuda, N., & Hanawa, T. 1999, *ApJ*, 517, 226
- Goldreich, P., & Sridhar, S. 1995, *ApJ*, 438, 763
- Goldstein, M. L. 1978, *ApJ*, 219, 700
- Goldstein, M. L., Roberts, D. A., & Matthaeus, W. H. 1995, *ARA&A*, 33, 283
- Grappin, R., Velli, M., & Mangeney, A. 1993, *Physical Review Letters*, 70, 2190
- Heinemann, M., & Olbert, S. 1980, *J. Geophys. Res.*, 85, 1311
- Hollweg, J. V. 1971, *J. Geophys. Res.*, 76, 5155
- . 1973, *J. Geophys. Res.*, 78, 3643
- Hollweg, J. V., & Isenberg, P. A. 2007, *Journal of Geophysical Research (Space Physics)*, 112, 8102
- Hollweg, J. V., Jackson, S., & Galloway, D. 1982, *Sol. Phys.*, 75, 35
- Hoshino, M., & Goldstein, M. L. 1989, *Physics of Fluids B*, 1, 1405
- Hossain, M., Gray, P. C., Pontius, Jr., D. H., Matthaeus, W. H., & Oughton, S. 1995, *Physics of Fluids*, 7, 2886
- Iroshnikov, P. S. 1964, *Soviet Ast.*, 7, 566
- Jacques, S. A. 1977, *ApJ*, 215, 942
- Kennel, C. F., Blandford, R. D., & Wu, C. C. 1990, *Physics of Fluids B*, 2, 253
- Kraichnan, R. H. 1965, *Physics of Fluids*, 8, 1385

- Kudoh, T., & Shibata, K. 1999, *ApJ*, 514, 493
- Matsumoto, T., & Shibata, K. 2010, *ApJ*, 710, 1857
- Matsumoto, T., & Suzuki, T. K. 2014, *MNRAS*, 440, 971
- Montgomery, D. 1959, *Physical Review Letters*, 2, 36
- Moriyasu, S., Kudoh, T., Yokoyama, T., & Shibata, K. 2004, *ApJ*, 601, L107
- Nakajima, Y., & Hanawa, T. 1996, *ApJ*, 467, 321
- Nariyuki, Y. 2015, *Physics of Plasmas*, 22, 022309
- Okamoto, T. J., et al. 2007, *Science*, 318, 1577
- Sagdeev, R. Z., & Galeev, A. A. 1969, *Nonlinear Plasma Theory*
- Stone, J. M., Gardiner, T. A., Teuben, P., Hawley, J. F., & Simon, J. B. 2008, *ApJS*, 178, 137
- Suzuki, T. K., & Inutsuka, S.-i. 2005, *ApJ*, 632, L49
- Suzuki, T. K., & Inutsuka, S.-I. 2006, *Journal of Geophysical Research (Space Physics)*, 111, 6101
- Tu, C.-Y., & Marsch, E. 1995, *Space Sci. Rev.*, 73, 1
- van Ballegooijen, A. A., Asgari-Targhi, M., Cranmer, S. R., & DeLuca, E. E. 2011, *ApJ*, 736, 3
- Velli, M. 1993, *A&A*, 270, 304
- Verdini, A., & Velli, M. 2007, *ApJ*, 662, 669
- Verdini, A., Velli, M., Matthaeus, W. H., Oughton, S., & Dmitruk, P. 2010, *ApJ*, 708, L116

Woolsey, L. N., & Cranmer, S. R. 2015, ApJ, 811, 136

Zank, G. P., & Matthaeus, W. H. 1992, Journal of Plasma Physics, 48, 85

Zhou, Y., & Matthaeus, W. H. 1990, J. Geophys. Res., 95, 10291